Intraplate volcanism originating from upwelling hydrous mantle transition zone

(Article begins on next page)

Intraplate volcanism originating from upwelling hydrous mantle transition zone

Jianfeng Yang, Manuele Faccenda*

Dipartimento di Geoscienze, Università di Padova, 35131 Padova, Italy

Most magmatism occurring on Earth is conventionally attributed to passive mantle upwelling at mid-ocean ridges, slab devolatilization at subduction zones, and mantle plumes. However, the widespread Cenozoic intraplate volcanism in northeast China[1-3] and the peculiar petit-spot volcanoes[4-7] offshore the Japan trench cannot be readily associated with any of these mechanisms. In addition, the mantle beneath this type of volcanism is characterized by seismic low velocity zones (LVZs) present above and below the transition zone[8-12], and a comprehensive interpretation of all these intriguing phenomena is lacking. Here we show that most if not all the intraplate and petit-spot volcanism and LVZs present around the Japanese subduction zone can be explained by the Cenozoic interaction of the subducting Pacific slab with a hydrous transition zone. Numerical modelling results indicate that 0.2-0.3 wt.% H_2O dissolved in mantle minerals which are driven out from the transition zone in response to subduction and retreat of a stagnant plate is sufficient to reproduce the observations. This suggests that a critical amount of water may have accumulated in the transition zone around this subduction zone as well as others of the Tethyan tectonic belt[13] characterized by intraplate/petit-spot volcanism and LVZs in the underlying mantle.

The Cenozoic intraplate volcanism in northeast China is located more than 1000 km westward of the Japan trench[1], while the young alkaline basalts (0-6 Ma) known as petit-spots outcrop up to 600 km eastward of the trench[4] (Fig. 1). The formation mechanism of these types of on- and off-shore volcanism is still debated as there is no geological and geophysical correlation with mantle plumes or arc volcanism[6,14].

Seismic tomography models indicate that in this region the Pacific Plate is currently stagnant in the transition zone, extending continuously up to nearly 1000 km to the inland of northeast China[3,8,10]. Thus, it has been proposed that the Cenozoic intraplate magmatism is related to the dehydration of the Pacific slab in the mantle transition zone (MTZ) between ~410 km and ~660 km depth[2,15].

The primary petit-spot magma has been determined volatile-rich with extremely EM 1-like isotopic compositions[6,7]. The lack of hotspot tracks in this region excludes the contribution from a mantle

35 plume. It has been postulated that the petit-spot magma forms in the asthenosphere, and migrates

36 upward through the oceanic lithosphere by reactive porous flow in response to plate flexure[4,6,7].

37

38 Based on electrical conductivity surveys, the transition zone probably holds circa 0.1 wt.% water[16],

39 while the transition zone below China and Japan are particularly wet with at least 0.5-1 wt.% water[17].

40 The MTZ is primarily composed of wadsleyite and ringwoodite minerals that can accommodate 1-3

41 wt.% water, which is 1 to 2 orders of magnitude higher than the water (hydrogen) solubility in upper

42 and lower mantle minerals. Given the large contrast in water solubility between the MTZ and

43 upper/lower mantle, it is reasonable to expect deep dehydration melting when subducting slabs excite

44 vertically flow in the nearby wet MTZ[18]. Indeed, seismic low velocity zones (LVZs) above 410 km

45 and below 660 km have been observed not only in Japan[8-12,14,15], but also around subduction zones in

46 Europe[19] and western US[20,21].

47

48 To test this hypothesis, we construct two-dimensional numerical experiments in which a self-

49 sustained oceanic plate subduction is characterized by trench retreat and slab stagnation into a

50 homogeneously or heterogeneously wet MTZ (Methods). The subducting plate and entrained dry

51 upper mantle push the adjacent wet MTZ downward to the lower mantle such that a partially molten

52 layer forms between 700 and 800 km depth (Fig. 2a, M2) (Supplementary Video 1). On the other

53 hand, MTZ material uplifted to the upper mantle starts to partially melt above 410-km (Fig. 2a, M3).

54 Slab stagnation and retreat is accompanied by subslab MTZ upwelling and new melting (M1). These

55 partially molten regions above and below the MTZ cause significant seismic LVZs (Fig. 2c). When

56 melt percolation is active (Methods), extraction to the surface occurs forming intraplate and petit-

57 spot volcanisms ahead of and behind the trench, respectively.

58

59 Figure 3 shows the spatial and temporal trend of modelled volcanics for the reference model in Fig.

60 2. The first intraplate volcanism occurs ~500 km away from the trench, then it spreads to two opposite

61 directions. The mantle water content decreases after melt extraction, which precludes further deep

62 (≥200 km) melting of the residual peridotite (Fig. 2b). As the slab rolls back, more distal wet MTZ is

63 sucked into the upper mantle wedge, such that partial melting and volcanoes will form further away

64 from the trench. The new generated volcanism is not homogeneously distributed as it is strongly

65 influenced by mantle flow and trench movement. Furthermore, a heterogeneous distribution of water

66 in the MTZ would prevent the formation of any temporal-spatial magmatic sequence as wetter

67 portions would melt earlier than drier regions at the same P-T conditions. It is noteworthy that

68 intraplate volcanism also occurs few hundred kilometers in front of the slab tip. At ~12 Myr, petit-

69 spot volcanoes behind the trench appear, they are located at the trench up to ~300 km far away and

70 exhibit a similar magmatic activity trend as the intraplate volcanism.

71

72 We further test the influence of initial water content in the transition zone and other parameters on

73 the genesis of asthenospheric melting (Extended Data Fig. 5). Melting commences 40 km above the

74 transition zone and no petit-spot volcanoes are formed for 0.2 wt.% initial water. The thickness of the

75 partially molten layer could be few tens of km to more than 100 km, depending on the melt extraction

76 efficiency and water content. Petit-spot volcano might locate more than 600 km away from the trench

77 if melt extraction process is readily efficient (Extended Data Fig. 5b). Given the assumed

78 homogeneous distribution of water in the MTZ, these models provide upper bound estimates on the

79 volumes of volcanics and melt. However, the results hold also in case of a more realistic

80 heterogeneous distribution of the water in this mantle level (Extended Data Fig. 5e).

81

82 When comparing the model results with seismic and geological observations, we note that around the

83 Pacific slab three remarkable seismic low velocity zones outward of the transition zone are clearly

84 imaged which are well correlated with the locations of intraplate and petit-spot volcanoes, and the

85 modelled partially molten zones (Figs. 1-2). Although seismic low velocity anomalies are generally

86 attributed to thermal effects[14], presence of water[22], melt[11,20] and/or major element compositional

87 heterogeneities[16,23], it has been recently argued that some of these LVZs could be seismic anisotropy-

88 induced artifacts[24]. Nevertheless, the authenticity of the subslab LVZ1 and LVZ2 appearing in

89 tomographic models have been confirmed by other independent studies using, respectively, an

90 accurate scrutiny of the seismic ray paths[25] sampling the LVZ1 and receiver functions[11]. The LVZ3

91 sits below the active Changbai volcano and appears to extend down to 410 km as clearly revealed by

92 multiple high-resolution tomography models[3,8,15,26]. A thermal anomaly from a non-hotspot

93 upwelling, if hypothetically exists, is hardly reconcilable with the large velocity drop of LVZ1. The

94 hot material will rapidly cool down when flowing upward by adiabatic decompression and the latent

95 heat of the wadsleyite to olivine reaction. Laboratory experiments show that seismic wave speeds are

96 insensitive to moderate (< 1wt. %) water contents for olivine[27] and wadsleyite[22], thus the LVZs are

97 very likely to be caused by partial melting and/or compositional heterogeneities. The presence of

98 basalts at the bottom of the upper mantle should be excluded as it would generate a positive seismic

99 anomaly[28]. On the other hand, basalts accumulating at the base of the MTZ could be effectively

100 dragged by the slab into the uppermost lower mantle and generate the LVZ2. However, receiver

101 functions indicate that the lower mantle LVZs are within the 750-780 km depth range[11], which is

102 likely below the post-garnet phase transition where basalts are seismically faster than mantle rocks.

104 The presence of melt in the deep mantle, which is mostly catalyzed by volatiles involvement, decreases seismic velocities and provides a magmatic source for intraplate/petit-spot volcanism. Our numerical models thereby suggest that a hydrous transition zone with at least 0.2-0.3 wt.% water beneath northeast China and offshore Japan can comprehensively explain the LVZs, and the intraplate and petit-spot volcanism. This model does not exclude the devolatilization of the stagnant Pacific slab as a mechanism to explain the LVZ3 region and the overlying intraplate volcanism[15], which favors the upwelling of volatile-rich plumes from the MTZ[29] as envisaged by the Big Mantle Wedge model[15,30]. However, the same slab-derived volatiles cannot obviously be the cause of the LVZ1 and LVZ2 and of the petit-spots, implying the presence of a metasomatized MTZ before the last subduction episode. The accumulation of water in the MTZ could be caused by, for example, delamination of volatile-rich lithospheric roots[31] or by previous slab dehydration episodes in the MTZ and subsequent absorption of the water by wadsleyite and ringwoodite. Alongside with water, reduced (by redox-freezing) carbonated sources and restitic, K-hollandite-bearing sediments are required to explain the volatile-rich, alkaline and EM1-type petrological and geochemical signature of the basalts[32,33]. This is not surprising since the MTZ, a graveyard for stagnating slabs, is the most likely candidate to host volatiles and subducted sediments, and long-term isolation of these MTZ domains would be consistent with the ancient metasomatizing episodes estimated for intraplate basalts[32-34]. Subsequent subduction events would mobilize the wet and (carbon + alkali)-bearing MTZ rocks promoting the formation of silica undersaturated magmas in the upper mantle. It is important to note that the addition of these components is not critical to our results because the location and amounts of partial melting atop and below the MTZ will still be dictated by the distribution of wet MTZ domains, while reduced carbonated sources are expected to experience redox melting at shallower depths (<250 km)[35]. The process proposed here could potentially explain also the Cenozoic anorogenic volcanism in the Mediterranean[13] and intraplate volcanism in the Turkish-Iranian Plateau[36] regions characterized by the long-term subduction of Tethys ocean. Together with surface intraplate/petit-spot volcanism, constraints on deep seismic low velocities and/or high electrical conductivity may thus indicate a volatile-rich and/or partially molten mantle within and around the transition zone.

Data availability The dataset generated during the current study are available at
https://figshare.com/articles/Yang_Faccenda_Nature2019/9933056.

Code availability Requests about the numerical modelling codes associated with this paper should be sent to the main code developer (taras.gerya@erdw.ethz.ch). The numerical 2D finite element code MVEP2 (https://bitbucket.org/bkaus/mvep2) was used for the two-phase flow model in Extended Data Figure 6.

References

1. Chen, Y., Zhang, Y., Graham, D., Su, S. & Deng, J. Geochemistry of Cenozoic basalts and mantle xenoliths in Northeast China. Lithos **96**, 108-126 (2007).

2. Wang, X.-C., Wilde, S. A., Li, Q.-L. & Yang, Y.-N. Continental flood basalts derived from the hydrous mantle transition zone. Nat. Commun. **6**, 7700 (2015).

3. Chen, C. et al. Mantle transition zone, stagnant slab and intraplate volcanism in Northeast Asia. Geophys. J. Int. **209**, 68-85 (2017).

4. Hirano, N. et al. Volcanism in response to plate flexure. Science **313**, 1426-1428 (2006).

5. Okumura, S. & Hirano, N. Carbon dioxide emission to Earth's surface by deep-sea volcanism. Geology **41**, 1167-1170 (2013).

6. Machida, S. *et al.* Petit-spot geology reveals melts in upper-most asthenosphere dragged by lithosphere. Earth Planet. Sci. Lett. **426**, 267-279 (2015).

7. Pilet, S. et al. Pre-subduction metasomatic enrichment of the oceanic lithosphere induced by plat flexure. Nat. Geosci. **9**, 898 (2016).

8. Li, C., Van der Hilst, R. D., Meltzer, A. S. & Engdahl, E. R. Subduction of the Indian lithosphere beneath the Tibetan Plateau and Burma. Earth Planet. Sci. Lett. **274**, 157-168 (2008).

9. Tauzin, B., Debayle, E. & Wittlinger, G. Seismic evidence for a global low-velocity layer within the Earth's upper mantle. Nat. Geosci. **3**, 718 (2010).

10. Fukao, Y. & Obayashi, M. Subducted slabs stagnant above, penetrating through, and trapped below the 660 km discontinuity. J. Geophys. Res.: Solid Earth **118**, 5920-5938 (2013).

11. Liu, Z., Park, J. & Karato, S.-i. Seismological detection of low velocity anomalies surrounding the mantle transition zone in Japan subduction zone. Geophys. Res. Lett. **43**, 2480-2487 (2016).

12. Wei, S. S. & Shearer, P. M. A sporadic low-velocity layer atop the 410 km discontinuity beneath the Pacific Ocean. J. Geophys. Res.: Solid Earth **122**, 5144-5159 (2017).

13. Lustrino, M. & Wilson, M. The circum-Mediterranean anorogenic Cenozoic igneous province. Earth Sci. Rev. **81**, 1-65 (2007).

14. Tang, Y. et al. Changbaishan volcanism in northeast China linked to subduction-induced mantle upwelling. Nat. Geosci. **7**, 470 (2014).

15. Zhao, D., tian, Y., Lei, J., Liu, L., Zheng, S. Seismic image and origin of the Changbai intraplate volcano in East Asia: Role of big mantle wedge above the stagnant Pacific slab. Phys. Earth Planet. Lett. **173**, 197-206 (2009).

16. Karato, S.-i. Water distribution across the mantle transition zone and its implications for global material circulation. Earth Planet. Sci. Lett. **301**, 413-423 (2011).

17. Kelbert, A., Schultz, A. & Egbert, G. Global electromagnetic induction constraints on transition-zone water content variations. Nature **460**, 1003 (2009).

18. Bercovici, D. & Karato, S.-i. Whole-mantle convection and the transition-zone water filter. Nature **425**, 39-44 (2003).

19. Liu, Z., Park, J. & Karato, S.-i. Seismic evidence for water transport out of the mantle transition zone beneath the European Alps. Earth Planet. Sci. Lett. **482**, 93-104 (2018).

20. Schmandt, B., Jacobsen, S. D., Becker, T. W., Liu, Z. & Dueker, K. G. Dehydration melting at the top of the lower mantle. Science **344**, 1265-1268 (2014).

21. Hier-Majumder, S. & Tauzin, B. Pervasive upper mantle melting beneath the western US. Earth Planet. Sci. Lett. **463**, 25-35 (2017).

22. Mao, Z. et al. Elasticity of hydrous wadsleyite to 12 GPa: implications for Earth's transition zone. Geophys. Res. Lett. **35** (2008).

23. Irifune, T. et al. Sound velocities of majorite garnet and the composition of the mantle transition region. Nature **451**, 814 (2008).

179 24. Bezada, M., Faccenda, M. & Toomey, D. Representing anisotropic subduction zones with isotropic velocity models: A
180 characterization of the problem and some steps on a possible path forward. Geochem. Geophys. Geosy. **17**, 3164-3189 (2016).
181 25. Obayashi, M., Sugioka, H., Yoshimitsu, J. & Fukao, Y. High temperature anomalies oceanward of subducting slabs at the 410-km
182 discontinuity. Earth Planet. Sci. Lett. **243**, 149-158 (2006).
183 26. Zhao, D. & Tian, Y. Changbai intraplate volcanism and deep earthquakes in East Asia: a possible link? Geophys. J. Int. **195**,
184 706-724 (2013).
185 27. Cline II, C. J., Faul, U. H., David, E. C., Berry, A. J. & Jackson, I. Redox-influenced seismic properties of upper-mantle olivine.
186 Nature **555**, 355 (2018).
187 28. Xu, W., Lithgow-Bertelloni, C., Stixrude, L. & Ritsema, J. The effect of bulk composition and temperature on mantle seismic
188 structure. Earth Planet. Sci. Lett. **275**, 70-79 (2008).
189 29. Litasov, K. D., Shatskiy, A., Ohtani, E. & Yaxley, G. M. Solidus of alkaline carbonatite in the deep mantle. Geology **41**, 79-82
190 (2013).
191 30. Kuritani, T. et al. Buoyant hydrous mantle plume from the mantle transition zone. Sci. Rep. **9**, 6549 (2019).
192 31. Green II, H. W., Chen, W.-P. & Brudzinski, M. R. Seismic evidence of negligible water carried below 400-km depth in
193 subducting lithosphere. Nature **467**, 828-831 (2010).
194 32. Mazza, S. E. et al. Sampling the volatile-rich transition zone beneath Bermuda. Nature **569**, 398-403 (2019).
195 33. Wang, X.-J. et al. Mantle transition zone-derived EM1 component beneath NE China: Geochemical evidence from Cenozoic
196 potassic basalts. Earth Planet. Sci. Lett. **465**, 16-28 (2017).
197 34. Kuritani, T., Ohtani, E. & Kimura, J. I. Intensive hydration of the mantle transition zone beneath China caused by ancient slab
198 stagnation. Nat. Geosci. **4**, 713-716 (2011).
199 35. Rohrbach, A. & Schmidt, M. W. Redox freezing and melting in the Earth's deep mantle resulting from carbon-iron redox
200 coupling. Nature **472**, 209 (2011).
201 36. Soltanmohammadi, A. et al. Transport of Volatile-rich Melt from the Mantle Transition Zone via Compaction Pockets: Implications
202 for Mantle Metasomatism and the Origin of Alkaline Lavas in the Turkish–Iranian Plateau. J. Petrol. **59**, 2273-2310 (2018).

203

208

209 **Author Contributions** M.F. conceived the study. J.Y. performed all the numerical experiments and
210 wrote the first draft of the paper. Both authors equally contributed to the discussion of the results and
211 to the conclusions of this study.

212 **Competing Interests** The authors declare no competing interests.
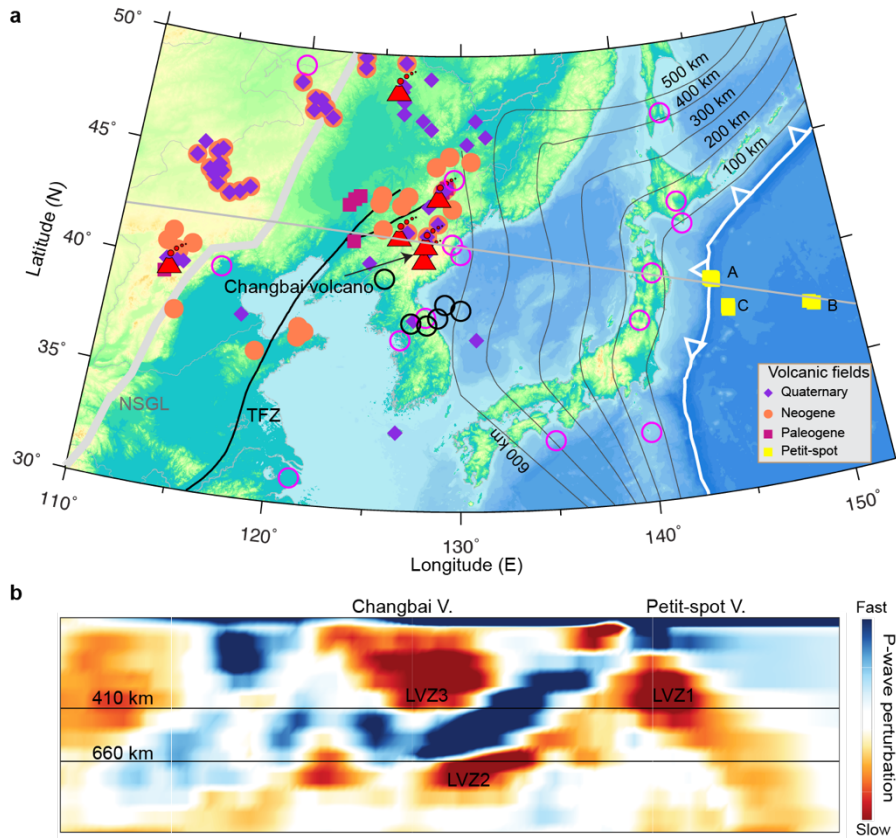
213 **Additional information**

214 **Extended data**

215 **Supplementary information**

216 **Reprints and permissions information** is available at www.nature.com/reprints

218

219

Figure 1 | Geological/Geophysical maps and Cenozoic volcanic fields in northeast China and offshore Japan. **a**, the red triangles denote volcanoes, the black and magenta circles show seismic low velocity at the 410 km and below 660 km, respectively, as determined by receiver functions[9,11,12]. Three young alkaline basalt sites (A, B, C) offshore the Japan trench known as petit-spot. The black contour lines indicate the Pacific Plate depths in the mantle. The present-day Pacific Plate front lies between the Tanlu Fault Zone (TFZ) and the North-South Gravity Lineament (NSGL). The map is created with open software GMT 5.4.3 which is under a GNU Lesser General Public License. **b**, cross-section (grey line in **a**) of seismic P-wave velocity perturbation with three distinct low velocity zones[8].
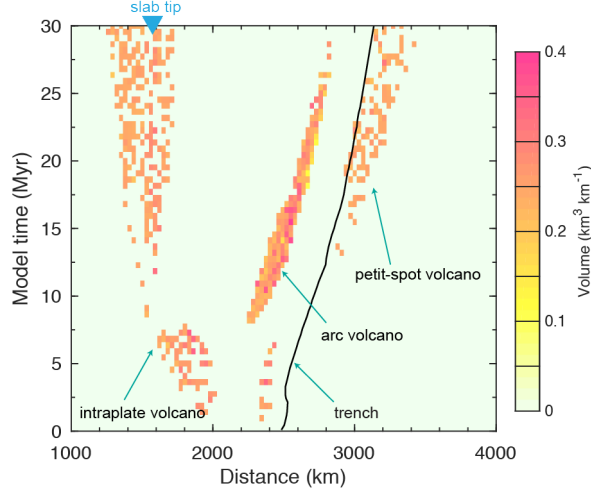
227
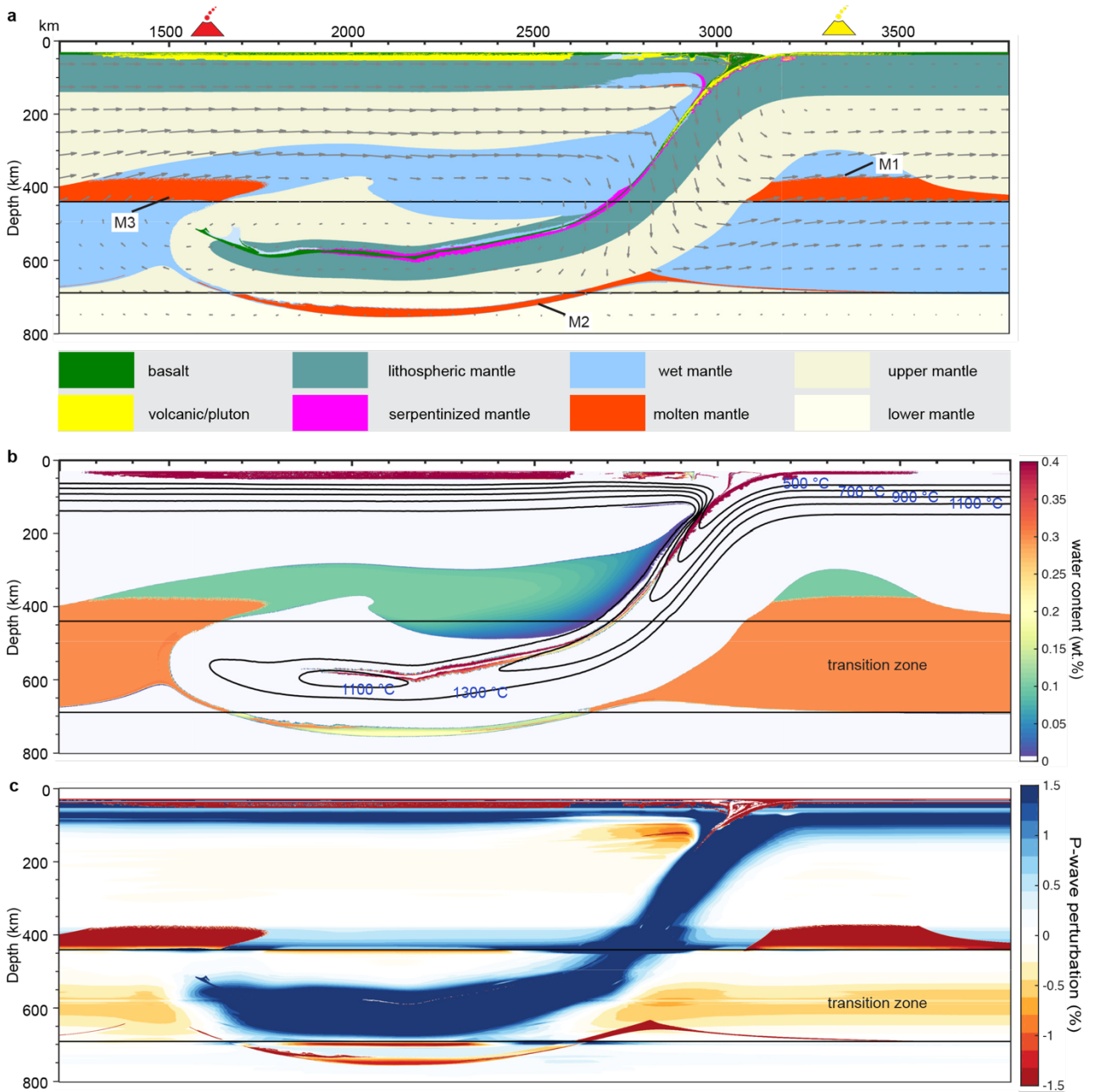
Figure 2 | Dynamics of subdution-induced dehydration melting above and below the transition zone. **a**, composition field and colors indicating different rock types at the bottom. Two black lines mark depths of 410-km and 660-km. Three partially molten regions (M) are indicated. **b**, water content with temperature contours and **c**, seismic P wave velocity anomalies. An initial water content of 0.3 wt.% is assumed in the MTZ and t_{ref}=6 kyr.

Figure 3 | Volcanics volume versus time. The volcanics include arc volcanoes by shallow decompression/hydrous melting and intraplate/petit-spot volcanoes by wet deep upper mantle melting. The trench location (black line) through the model evolution and the final location of the slab tip (inverted blue triangle) are also indicated.

Methods

Modelling approach. The 2-D petrological-thermo-mechanical numerical code I2VIS used in this study is based on a finite difference method employing marker-in-cell technique on a staggered grid[37]. It solves mass, momentum and energy conservation equations (eq. 1-3) on the Eulerian grid, and interpolates physical properties to the markers for advection accordingly.

$$\frac{\partial v_i}{\partial x_i} = 0 \tag{1}$$

$$-\frac{\partial P}{\partial x_i} + \frac{\partial}{\partial x_j}\left(\eta\left(\frac{\partial v_i}{\partial x_j} + \frac{\partial v_j}{\partial x_i}\right)\right) + \rho g_i = 0 \tag{2}$$

$$\rho c_p\left(\frac{\partial T}{\partial t} + v_i\frac{\partial T}{\partial x_i}\right) = \frac{\partial}{\partial x_i}\left(k\frac{\partial T}{\partial x_i}\right) + H_r + H_s + H_a \tag{3}$$

where v_i is velocity, x_i coordinate, P dynamic pressure, ρ density, g gravity acceleration, c_p heat capacity, T temperature, k thermal conductivity, H_r radioactive heating, $H_s = \tau_{ij}\dot{\varepsilon}_{ij}$ shear heating and adiabatic heating $H_a = T\alpha\frac{DP}{Dt}$. The latent heat is implicitly considered by computing the effective thermal expansion and heat capacity.

Model configuration. The initial model setup (6000 × 1000 km discretized with 1501 × 501 nodes) is composed of a 3500 km subducting plate and a 2500 km overriding plate. The model imposes free-slip mechanical boundary condition at the top with 30-km-thick and viscosity of 10^{18} Pa s 'sticky-air' to mimic free surface; the bottom boundary is no slip, and side boundaries are periodic. The bottom no-slip condition is needed to define an initial horizontal velocity from which finite differences can be computed for this variable. Comparison with results from a model with bottom free-slip condition

9

258 and closed vertical walls indicate that the bottom no-slip boundary condition does not affect at all the
259 subduction dynamics as it is confined above the lower mantle. The initial thermal structure is defined
260 by the half-space cooling age for the plates (50 Myr old) and an adiabatic thermal gradient of 0.5
261 K/km for the underlying mantle. The thermal boundary conditions are isothermal on the top and
262 bottom, while side boundaries are periodic consistently with the mechanical boundary conditions. To
263 initiate subduction, the subducting slab extends down to ~200 km in the upper mantle together with
264 a rheologically weak zone on top of it which lubricate the initial plates contact. The employed high
265 numerical resolution (4 km × 2 km) is needed to ensure plate contact lubrication at shallow depths
266 and localized, bending-related hydration at the trench outer-rise. Tests with a lower resolution (4 km
267 × 4 km) results in a less localized slab mantle hydration, while with an 8 km × 4 km resolution self-
268 sustained subduction and slab rollback do not appear spontaneously.

269

270 **Viscous-plastic rheological model**. The rock mechanical behaviour is represented by the effective
271 viscosity which combines ductile (dislocation, diffusion and Peierls creep) and brittle (Drucker-
272 Prager) deformation. The effective ductile viscosity is given by the harmonic average of the combined
273 rheologies (parameters and physical meaning are defined in Extended Data Table 1):

274 $$\eta_{ductile} = (\frac{1}{\eta_{disl}} + \frac{1}{\eta_{diff}} + \frac{1}{\eta_{Peierls}})^{-1} \tag{4}$$

275 where the dislocation and diffusion creep are given by[38]:

276 $$\dot{\varepsilon} = A(\sigma/\mu)^n(b/d)^m \exp\left(-\frac{E+PV}{RT}\right) \exp(\alpha\phi) \tag{5}$$

277 $$\eta = \frac{\sigma}{2\dot{\varepsilon}} \tag{6}$$

278 For hydrated (wet) mantle, viscosity is reduced by $\eta_{wet} = \eta_{dry}\left(\frac{C_w}{C_{w0}}\right)^{-r/n}$, and C_w, C_{w0} are water
279 content and reference water content (100 ppm, which is the water content for the dry upper mantle),
280 respectively.

281 The Peierls creep is given by[39]:

282 $$\eta_{Peierls} = 0.5A_p\sigma_{II}'^{-1}\exp\left(\frac{E_{Peierls}+PV_{Peierls}}{RT}(1-(\frac{\sigma_{II}'}{\sigma_{Peierls}})^p)^q\right) \tag{7}$$

283 Brittle behaviour occurs when stresses are above the plastic yield stress τ_y:

284 $$\eta_{ductile} \leq \frac{\tau_y}{2\dot{\varepsilon}_{II}} \tag{8}$$

285 $$\tau_y = C + \mu P \tag{9}$$

286

287 **Petrological modelling**. Petrological solid-solid phase changes are included through the density and
288 enthalpy look-up tables for basalt and pyrolite obtained from PERPLE_X[40]. Therefore, major phase
289 transition boundaries at 410 km and 660 km have been considered.

10

290

291   The solidus ($T_s = f(P, T, H_2O)$) and liquidus ($T_l = f(P, T)$) temperatures for the upper mantle and

292   MTZ are taken from high-pressure experiments[41] (Extended Data Fig. 1). At lower mantle conditions

293   T_s and T_l vary considerably among different experiments. Here we adopt the dry solidus and liquidus

294   of chondritic mantle[43] which are relatively more compatible with the results of KLB-1 peridotite[44],

295   while the wet solidus[45] was measured on samples with an estimated water content of 400 ppm wt.

296

297   A conservative estimate of the melt fraction in the wet upper mantle[18] is applied:

298      $\phi = \dfrac{W_a - W_{ol}}{W_m - W_{ol}}$ (10)

299   where W_a, W_{ol} and W_m (10 wt. %) are water mass fraction of the ambient mantle, olivine and melt,

300   respectively. Note that the water solubility in olivine increases with pressure, therefore the melt

301   fraction will decrease with depth if W_a remains constant (Extended Data Fig. 3).

302

303   The silicate melt density (Extended Data Fig. 2) is from high-pressure sink-float experiments[53], which

304   show that melt density becomes denser than the surrounding mantle at around 400 km[53,54] due to the

305   increased compressibility. However, the presence of water generally reduces melt density that is

306   buoyant relative to solid mantle (see Extended Data Fig. 2), rendering melt extraction at this depth

307   possible. Moreover, we also test the melt density from molecular dynamics simulations at high

308   pressure conditions[56] (Extended Data Fig. 4f, 5d).

309

310   **Melt extraction timescale**. The distance over which the compaction rate decreases by a factor of e

311   is the characteristic length scale of the compaction process and is known as compaction length δ_c:

312      $\delta_c = \sqrt{\dfrac{K(\zeta + \frac{4}{3}\eta)}{\eta_f}}$ (11)

313   where ζ and η are the effective bulk and shear viscosities, respectively, of the partially molten rock;

314   η_f the fluid viscosity; K the permeability given by the empirical equation:

315      $K = K_0 (\dfrac{\phi}{\phi_0})^n$ (12)

316   where ϕ is the porosity (melt fraction); K_0 ($10^{-12}\ m^2$) the permeability at the reference porosity

317   ϕ_0 (0.01), and n =3.

318   The relative migration velocity between the melt and the solid matrix is w:

319      $w = \dfrac{K\Delta\rho g}{\eta_f \phi}$ (13)

320   thus, the extraction timescale t:

$$321 \quad t = \frac{\delta_c}{w} = \frac{\phi}{\Delta\rho g} \sqrt{\frac{\eta_f(\zeta + \frac{4}{3}\eta)}{K}} \tag{14}$$

322   where $\zeta \approx \frac{\eta}{\phi}$, so $\zeta + \frac{4}{3}\eta \approx \frac{\eta}{\phi}$; if $\eta_f = 1\ Pa \cdot s$, then

$$323 \quad t \approx \frac{1000}{\Delta\rho g \phi} \sqrt{\eta} \tag{15}$$

324   where $\Delta\rho$ is the density difference between the solid and melt, ranging from ~-100 to 270 kg/m^3

325   and typically ~70-180 kg/m^3 in the lowermost upper mantle if most of water is partitioned into melt,

326   and the surrounding mantle viscosity $\eta = 10^{19} - 10^{20} Pa \cdot s$ in the upper mantle. For melt fraction

327    $\phi = 0.02$, the estimated timescale would be $t_{ref} \approx$3-20 kyr. Note that this timescale is not the time for

328   melt migration to the surface, but only illustrates the efficiency of melt segregation from the solid

329   matrix and the likelihood of its emplacement at shallow depths. Indeed, a small migration time

330   implies a large $\Delta\rho$ (i.e., high buoyancy force) and/or high melt fraction (i.e., high permeability) and/or

331   weak solid matrix which can be easily deformed during compaction/decompaction processes. In this

332   study, we use a reference value t_{ref}=6 kyr. Melt extraction does not only depend on these three

333   parameters (and fluid viscosity), but also on the dihedral angle (i.e., melt interconnectivity). Previous

334   experiments showed that the dihedral angle decreases systematically with increasing pressure such

335   that it probably allows for complete wetting at ~400 km[61] where the dihedral angle is <5°[62]. At these

336   depths, melt interconnectivity is high even for low amounts of melt (<1%), which makes melt

337   extraction possible provided the extraction timescale is sufficiently low. As such, when the extraction

338   timescale t is smaller than t_{ref}, the material is extracted at the surface forming plutonic intrusions or

339   volcanics[63]. Note that when the melt density is larger than solid surrounding mantle between 11.5 and

340   13.5 GPa when water content is low[53] (Extended Data Fig. 2b), there will be no melt extraction. In

341   these conditions, the denser melt should percolate downward and accumulate over the 410-km

342   discontinuity[18]. However, dry melting is generally not occurring at ambient mantle conditions except

343   for an abnormal heat source associated with a mantle plume. As hydrogen partition preferentially into

344   the melt, the water content in the melt would be quite high decreasing its density[53,54,62]. As a result,

345   hydrous melt should be less dense than the solid matrix throughout the upper mantle[53].

346

347   The melt migration process is here illustrated with more realistic models accounting for visco-elasto-

348   plastic deformation in a two-phase flow regime. These models demonstrate that melt migration from

349   the deep upper mantle to the surface should occur through several mechanisms: viscous diapirism,

350   viscoplastic decompaction channels and elasto-plastic dyking[64,65] (Extended Data Fig. 6). For a weak

351   host rocks where viscous deformation dominates, such as asthenosphere, magma migrates by

352   diapirism. When the magma moves through the lithosphere-asthenosphere boundary (or the lower

353   crust in continents) where both ductile and brittle deformation occur, the fluid compaction pressure

354 might reach the tensile strength and magma migrates by channeling. If the host rock is completely

355 elasto-plastic, such as the core of lithospheric mantle and upper crust, magma migrates by dyking.

356

357 **Water budget.** The phase diagram reporting the maximum water content that can be hosted in

358 hydrated or wet (i.e., absorbed by Nominally Anhydrous Minerals, NAMs) mantle rocks is built upon

359 the compilation from refs 41, 55 (Extended Data Fig. 3). It is often assumed that heterogeneously

360 serpentinized mantle rocks below the oceanic Moho can contain up to 2 wt. % H_2O[66,67]. As such, the

361 maximum water content in hydrated rocks[55] is scaled accordingly.

362

363 As the oceanic crust completely dehydrates at about 300 km depth[41] generating fluids that fuel arc-

364 volcanism only, we assume a dry crust for the sake of simplicity. On the other hand, dehydration of

365 the underlying mantle within the transition zone is thought to cause intracontinental magmatism[15].

366 Consequently, we allow for serpentinization by bending-related deformation when the strain of

367 mantle rocks is greater than 0.1[67].

368

369 When the rock water content exceeds the saturation limit, decomposition of hydrous minerals or water

370 exsolution in NAMs occurs and fluid markers are generated and migrate according to the Darcy's

371 law[67,68] until they are absorbed by dry markers:

372 $$V_i^f = V_i^s - \frac{\nabla P - \rho_f g_i}{(\rho_s - \rho_f) g_y} V_0 \tag{16}$$

373 where V_i^s, V_i^f, are velocities of solid and fluid phases, respectively; ρ_s, ρ_f are densities of solid and

374 fluid, respectively; V_0 is a constant percolation velocity.

375

376 Upon partial melting and extraction, the water is partitioned into the extracted melt and water in the

377 residual peridotite as:

378 $$C_w^{melt} = \frac{C_w}{\phi(1-D)+D} \tag{17}$$

379 $$C_w^{res} = \frac{C_w - \phi C_w^{melt}}{(1-\phi)} \tag{18}$$

380 where $D = 0.01$ is the hydrogen partition coefficient for olivine polymorphs.

381

382 **Falling block tests.** The validity of the employed petrological model can be easily tested with a

383 simple model that a falling block (simulating the subducting slab) sinks into the wet MTZ exciting

384 wet upwellings to the upper mantle and squeezing water into the lower mantle (Extended Data Fig.

385 4). These tests indicate that the melt layer gets thicker (>100 km) when melt extraction is not efficient

386 owing to very small amounts of melt/water and/or denser melt phase. This might explain thick low

387   velocity layers above the 410 km in many regions[9]. After melt extraction, less water remains above

388   the transition zone causing higher viscosity and less melt fraction, which yields larger extraction

389   timescale, i.e., the melt is preferentially ponding above the 410-km depth.

390

391   **Seismic velocity anomalies**. The seismic velocity perturbation in Fig. 2c have been computed as:

392     $$\delta \ln V = \frac{V - V_{ref}}{V_{ref}} \qquad (19)$$

393   where V_{ref} is the average seismic velocity at specific depth.

394   The change of seismic wave velocities caused by the existence of a fluid phase is given by:

395     $$\frac{V_s}{V_s^0} = \frac{\sqrt{N/\mu}}{\sqrt{\bar{\rho}/\rho}} \qquad (20)$$

396     $$\frac{V_p}{V_p^0} = \frac{\sqrt{\frac{K_{eff}}{k} + (4\gamma/3)N/\mu}}{\sqrt{1 + 4\gamma/3}\sqrt{\bar{\rho}/\rho}} \qquad (21)$$

397   where

398     $$\frac{K_{eff}}{k} = \frac{K_b}{k} + \frac{(1 - K_b/k)^2}{1 - \phi - K_b/k + \phi k/k_f} \qquad (22)$$

399   and $\gamma = \frac{\mu}{k} = \frac{3(1-2\upsilon)}{2(1+\upsilon)}$, V_s^0, V_p^0 are the shear and compressional wave velocities of the solid phase; k,

400   μ, υ and ρ are bulk modulus, shear modulus, Poisson's ratio and density of solid phase, respectively.

401     $\bar{\rho} = (1 - \phi)\rho + \phi\rho_f$ is the effective density when fluid (e.g., melt) exists and the fluid density ρ_f.

402   K_b and N are bulk and shear moduli which are dependent on melt fraction, dihedral angle[69]:

403     $$K_b = (1 - \phi)k(1 - (1 - \varphi)^{n_k}) \qquad (23)$$

404     $$N = (1 - \phi)\mu(1 - (1 - \varphi)^{n_\mu}) \qquad (24)$$

405   where

406     $$n_k = a_1\varphi + a_2(1 - \varphi) + a_3\varphi(1 - \varphi)^{1.5} \qquad (25)$$

407     $$n_\mu = b_1\varphi + b_2(1 - \varphi) + b_3\varphi(1 - \varphi)^2 \qquad (26)$$

408   and φ is the dihedral angle

409     $$\varphi = \frac{2A_{ss}}{2A_{ss} + A_{sl}} \qquad (27)$$

410   and A_{ss}, A_{sl} are the area of solid-solid contact and solid-liquid contact, respectively[70].

411

412   Extended Data Fig. 7 shows K_b/k and N/μ for the equilibrium geometry model at various dihedral

413   angles.

414

415   **Methods references**

416   37. Gerya, T. V. & Yuen, D. A. Characteristics-based marker-in-cell method with conservative finite-differences schemes for

417   modeling geological flows with strongly variable transport properties. Phys. Earth Planet. Inter. **140**, 293-318 (2003).

418 38. Karato, S.-i. & Wu, P. Rheology of the upper mantle: A synthesis. Science **260**, 771-778 (1993).

419 39. Kameyama, M., Yuen, D. A. & Karato, S.-I. Thermal-mechanical effects of low-temperature plasticity (the Peierls mechanism)

420 on the deformation of a viscoelastic shear zone. Earth Planet. Sci. Lett. **168**, 159-172 (1999).

421 40. Connolly, J. Computation of phase equilibria by linear programming: a tool for geodynamic modeling and its application to

422 subduction zone decarbonation. Earth Planet. Sci. Lett. **236**, 524-541 (2005).

423 41. Litasov, K. Physicochemical conditions for melting in the Earth's mantle containing a C–O–H fluid (from experimental data).

424 Russ. Geol. Geophys. **52**, 475-492 (2011).

425 42. Litasov, K. D. & Ohtani, E. Phase relations in hydrous MORB at 18–28GPa: implications for heterogeneity of the lower mantle.

426 Phys. Earth Planet. Inter. **150**, 239-263 (2005).

427 43. Andrault, D. et al. Melting of subducted basalt at the core-mantle boundary. Science **344**, 892-895 (2014).

428 44. Zhang, J. & Herzberg, C. Melting experiments on anhydrous peridotite KLB-1 from 5.0 to 22.5 GPa. J. Geophys. Res.: Solid

429 Earth **99**, 17729-17742 (1994).

430 45. Nomura, R. et al. Low core-mantle boundary temperature inferred from the solidus of pyrolite. Science, **343**, 522-525 (2014).

431 46. Pradhan, G. K. et al. Melting of MORB at core–mantle boundary. Earth Planet. Sci. Lett. **431**, 247-255 (2015).

432 47. Andrault, D. et al. Solidus and liquidus profiles of chondritic mantle: Implication for melting of the Earth across its history. Earth

433 Planet. Sci. Lett. **304**, 251-259 (2011).

434 48. Andrault, D. et al. Deep and persistent melt layer in the Archaean mantle. Nat. Geosci. **11**, 139 (2018).

435 49. Fiquet, G. et al. Melting of peridotite to 140 gigapascals. Science **329**, 1516-1518 (2010).

436 50. Boukaré, C. E., Ricard, Y. & Fiquet, G. Thermodynamics of the MgO-FeO-SiO2 system up to 140 GPa: Application to the

437 crystallization of Earth's magma ocean. J. Geophys. Res.: Solid Earth **120**, 6085-6101 (2015).

438 51. Baron, M. A. et al. Experimental constraints on melting temperatures in the MgO–SiO2 system at lower mantle pressures. Earth

439 Planet. Sci. Lett. **472**, 186-196 (2017).

440 52. Walter, M. J. et al. The stability of hydrous silicates in Earth's lower mantle: Experimental constraints from the systems MgO–

441 SiO2–H2O and MgO–Al2O3–SiO2–H2O. Chem. Geol. **418**, 16-29 (2015).

442 53. Sakamaki, T., Suzuki, A. & Ohtani, E. Stability of hydrous melt at the base of the Earth's upper mantle. Nature **439**, 192-194 (2006).

443 54. Jing, Z. & Karato, S.-i. Effect of H2O on the density of silicate melts at high pressures: Static experiments and the application of

444 a modified hard-sphere model of equation of state. Geochim. Cosmochim. Acta **85**, 357-372 (2012).

445 55. Iwamori, H. Phase relations of peridotites under H2O-saturated conditions and ability of subducting plates for transportation of

446 H2O. Earth Planet. Sci. Lett. **227**, 57-71 (2004).

447 56. Guillot, B. & Sator, N. A computer simulation study of natural silicate melts. Part II: High pressure properties. Geochim.

448 Cosmochim. Acta **71**, 4538-4556 (2007).

449 57. Sanloup, C. et al. Structure and density of molten fayalite at high pressure. Geochim. Cosmochim. Acta **118**, 118-128 (2013).

450 58. Bajgain, S., Ghosh, D. B. & Karki, B. B. Structure and density of basaltic melts at mantle conditions from first-principles

451 simulations. Nat. Commun. **6**, 8578 (2015).

452 59. Agee, C. B. Crystal-liquid density inversions in terrestrial and lunar magmas. Phys. Earth Planet. Inter. **107**, 63-74 (1998).

453 60. Petitgirard, S. et al. Fate of MgSiO3 melts at core–mantle boundary conditions. Proc. Natl. Acad. Sci. **112**, 14186-14190 (2015).

454 61. Yoshino, T., Nishihara, Y. & Karato, S.-i. Complete wetting of olivine grain boundaries by a hydrous melt near the mantle

455 transition zone. Earth Planet. Sci. Lett. **256**, 466-472 (2007).

456 62. Freitas, D. et al. Experimental evidence supporting a global melt layer at the base of the Earth's upper mantle. Nat. Commun. **8**,

457 2186 (2017).

458 63. Sizova, E., Gerya, T., Brown, M. & Perchuk, L. Subduction styles in the Precambrian: Insight from numerical experiments.

459 Lithos **116**, 209-229 (2010).

460 64. Keller, T., May, D. A. & Kaus, B. J. P. Numerical modelling of magma dynamics coupled to tectonic deformation of lithosphere

461 and crust. Geophys. J. Int. **195**, 1406-1442 (2013).

462 65. Lehmann, R. Modelling of Magma Dynamics from the Mantle to the Surface, Universitätsbibliothek Mainz (2016).

463   66. van Keken, P. E., Hacker, B. R., Syracuse, E. M. & Abers, G. A. Subduction factory: 4. Depth-dependent flux of H2O from

464   subducting slabs worldwide. J Geophys Res.: Solid Earth **116** (2011).

465   67. Faccenda, M., Gerya, T. V. & Burlini, L. Deep slab hydration induced by bending-related variations in tectonic pressure. Nat.

466   Geosci. **2**, 790-793 (2009).

467   68. Faccenda, M., Gerya, T. V., Mancktelow, N. S. & Moresi, L. Fluid flow during slab unbending and dehydration: Implications for

468   intermediate-depth seismicity, slab weakening and deep water recycling. Geochem. Geoph.y Geosy. **13** (2012).

469   69. Takei, Y. Effect of pore geometry on Vp/Vs: From equilibrium geometry to crack. J. Geophys. Res.: Solid Earth **107**,6-12

470   (2002).

471   70. Bargen, N. & Waff, H. S. Permeabilities, interfacial areas and curvatures of partially molten systems: results of numerical

472   computations of equilibrium microstructures. J. Geophys. Res.: Solid Earth **91**, 9261-9276 (1986).

473

474   **Extended Data Table 1** | Physical properties of rocks used in this study.

Property	Symbol	Unit	Value
Gravity	g	m/s^2	9.81
Water content	C_w	wt. %	-
Reference water content	C_{w0}	wt. %	0.01
Melt fraction	ϕ	-	-
Melt-weakening factor	α	-	28
Shear modulus	μ	GPa	80
Diffusion creep			
prefactor	A	s^{-1}	8.7×10^{15}
Activation energy	E	kJ mol^{-1}	300
Activation volume	V	cm^3 mol^{-1}	6
Burgers vector	b	nm	0.5
Grain-size exponent	m	-	2.5
Water exponent	r	-	0.8
Dislocation creep			
prefactor	A	s^{-1}	3.5×10^{22}
Activation energy	E	kJ mol^{-1}	540
Activation volume	V	cm^3 mol^{-1}	20
Stress exponent	n	-	3.5
Water exponent	r	-	1.2
Peierls creep			
prefactor	A_P	Pa^2 s	$10^{4.2}$
Activation energy	E_{Peis}	kJ mol^{-1}	532
Activation volume	V_{Peis}	cm^3 mol^{-1}	12
Peierls stress	σ_{Peis}	GPa	9.1
Exponent	p, q	-, -	1, 2
Yield stress τ_y			
Cohesion	C	MPa	10
Friction coefficient	μ	-	0.6

475
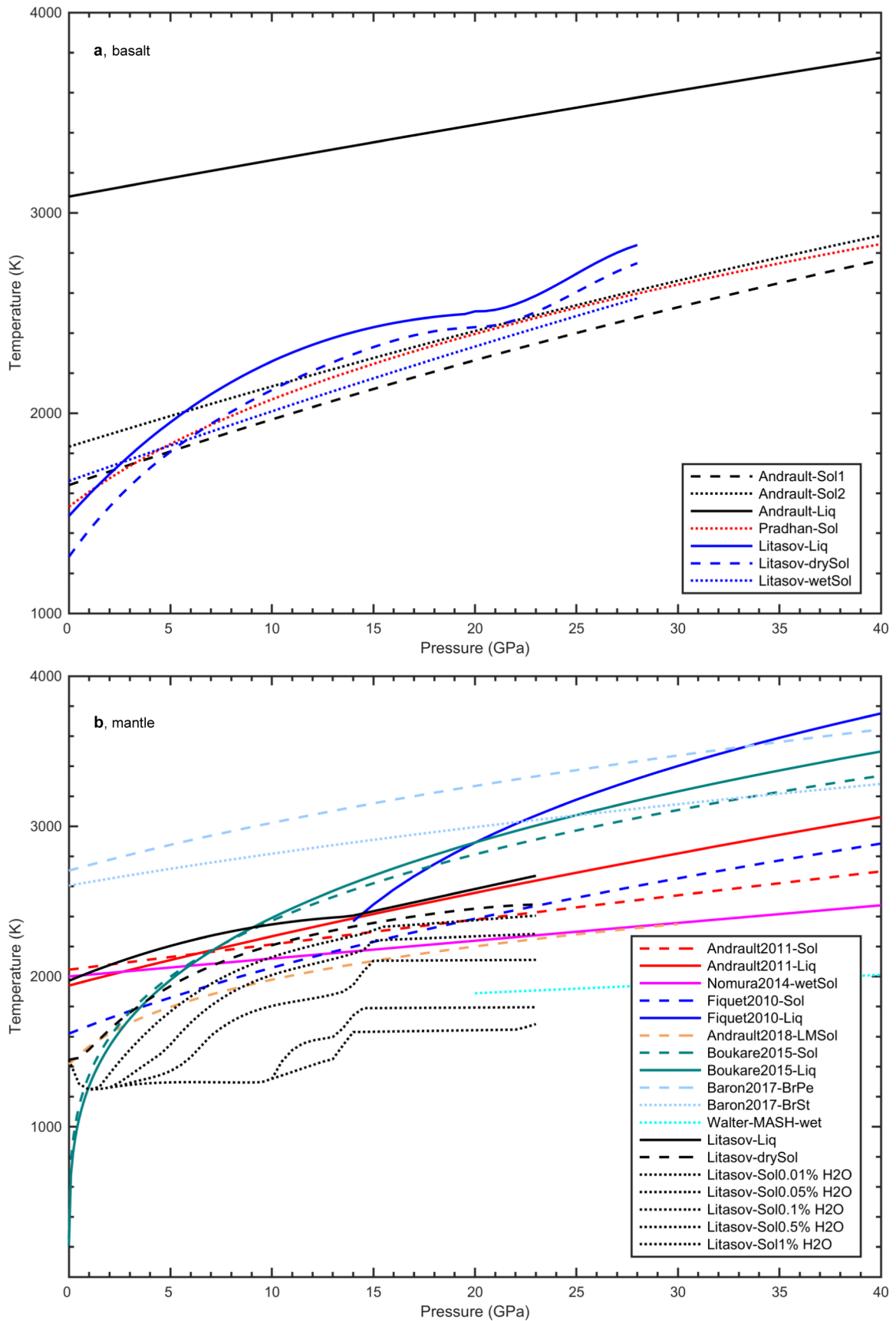
Extended Data Figure 1 | Solidus and liquidus of basalt and mantle. (a) The solidus and liquidus of basalt are obtained from experimental data[42,43,46]. The solidus from ref. 46 fits well within the uncertainty region by ref. 43 which is thus adopted. **(b)** Solidus and/or liquidus of mantle collected from literatures. The legends: *Sol*-solidus, *Liq*-liquidus, *BrPe*-

480 MgSiO₃-MgO (Bridgmanite + Periclase), *BrSt*-MgSiO₃-SiO₂ (Bridgmanite + Stishovite). Experimental data are from refs

481 41, 45, 47-52.

482

483

490

491

492 **Extended Data Figure 3 | Phase diagram of H_2O-peridotite after ref. 55.** The solidus/liquidus curves are the same in

493 Extended Data Fig. 1. The grey lines are olivine-wadsleyite (Ol-Wd) and ringwoodite-perovskite (Rd-Pv) phase

494 boundaries. The abbreviations of major hydrous phases are as follows: Chl-chlorite, Serp-serpentine, A-phase A, E-phase

495 E, shyB-superhydrous phase B, D-phase D.

496
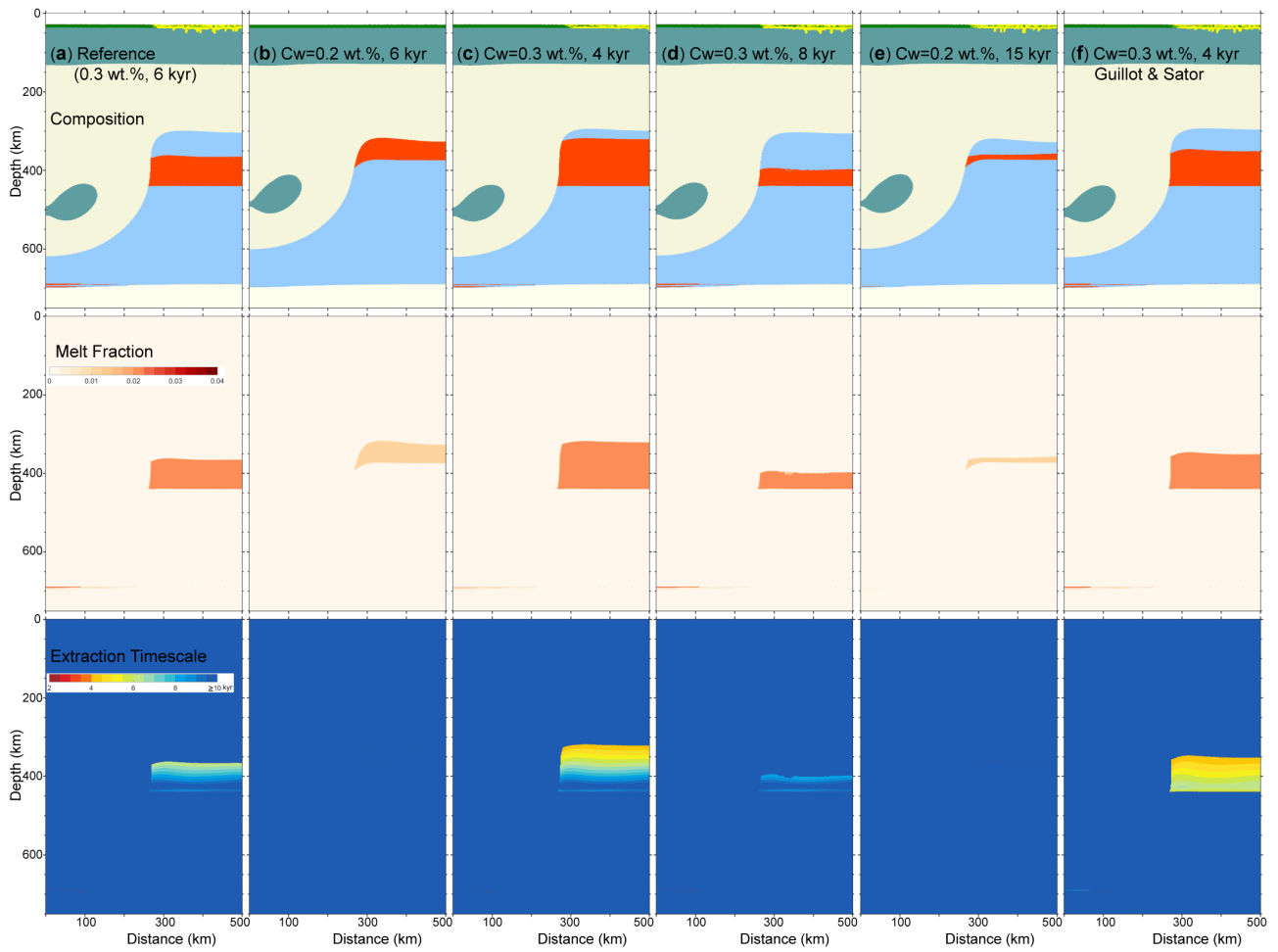
**Extended Data Figure 4 | Falling block simulations with different parameters.** (**a**) Reference model with initial MTZ water content of 0.3 wt.%, melt density from ref. 53 and reference extraction timescale t_{ref}=6 kyr. Other tests are similar to this model except for (**b**) initial water content Cw=0.2 wt.%, (**c**) extraction timescale t_{ref}=4 kyr, (**d**) t_{ref}=8 kyr, (**e**) Cw=0.2 wt.% and t_{ref}=15 kyr, (**f**) Cw=0.3 wt.% and t_{ref}=4 kyr by using the melt density from ref. 56. Note that the extraction timescale is calculated only when the melt is less dense than the solid matrix.
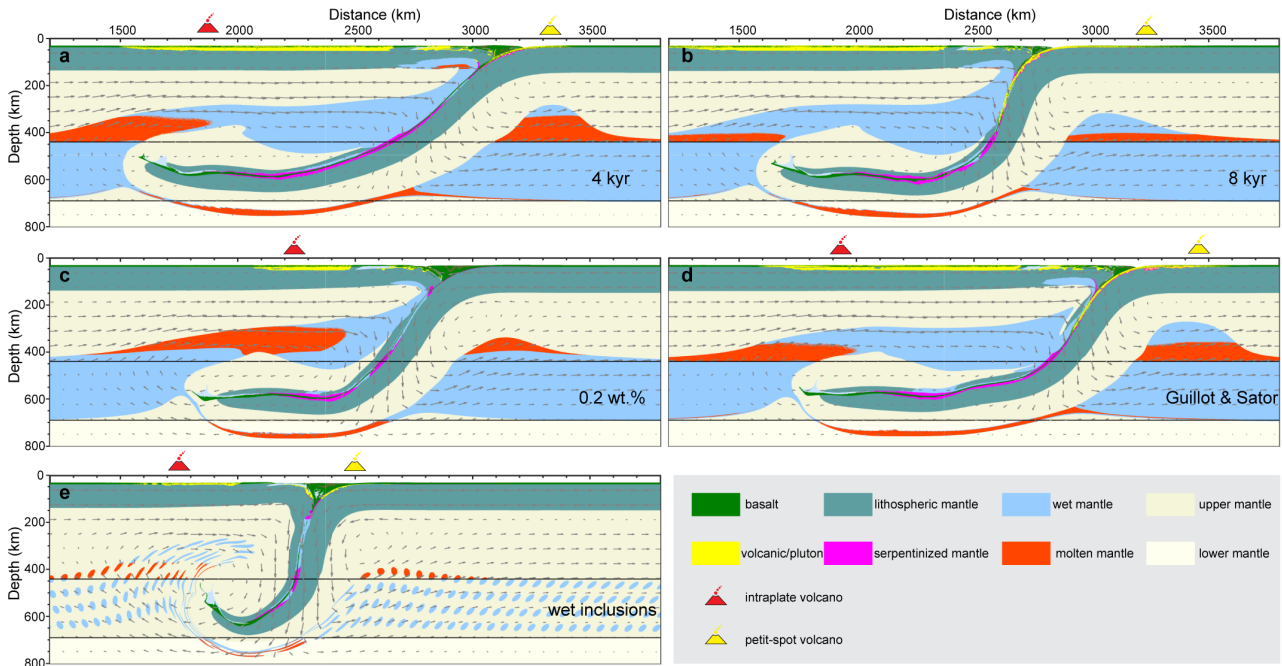
Extended Data Figure 5 | Additional parameter tests. Extraction timescale of 4 kyr in (**a**) and 8 kyr in (**b**) with 0.3 wt.% initial water content. A 0.2 wt.% initial water content in (**c**). Melt density from ref. 56 and t_{ref}=4 kyr in (**d**). (**e**), wet inclusions in the transition zone with t_{ref}=6 kyr. Note that all the models differ by only one particular parameter compared to the reference model (Fig. 2) except (**d**).
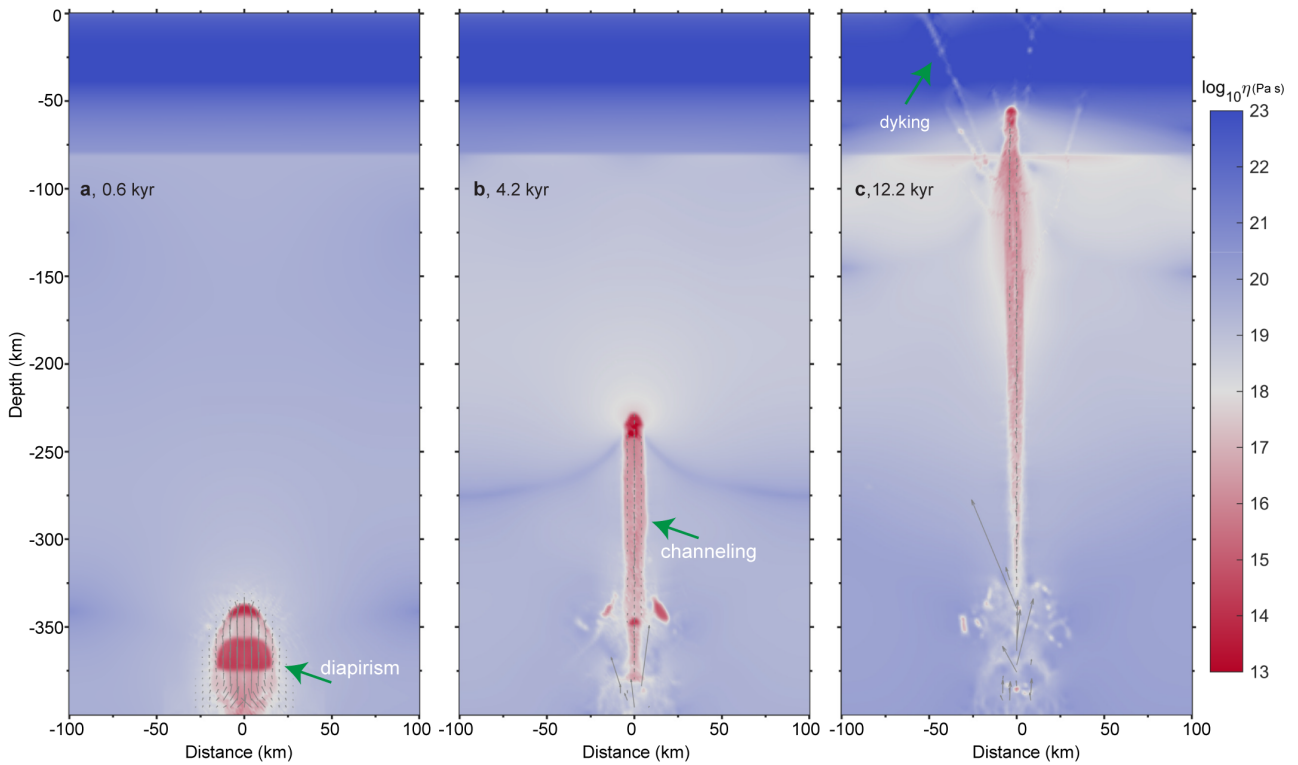
Extended Data Figure 6 | Visco-plastic shear viscosity for melt percolation in two-phase flow. Melt percolation at three typical stages as (**a**), diapirism (**b**), channeling and (**c**), dyking from deep mantle to the surface. The numerical 2D finite element code MVEP2 (https://bitbucket.org/bkaus/mvep2) was used to simulate melt migration dynamics. A small background strain rate (10^{-15} s^{-1}, the model domain has been extended by only 0.75 km after 12.2 kyr) was applied at the

side boundaries and top boundary is free surface. An initial porosity at the bottom boundary with Gaussian distribution (results in an average porosity of 0.127) was applied. The details of the approach allowing for its reproduction are provided elsewhere[64,65].
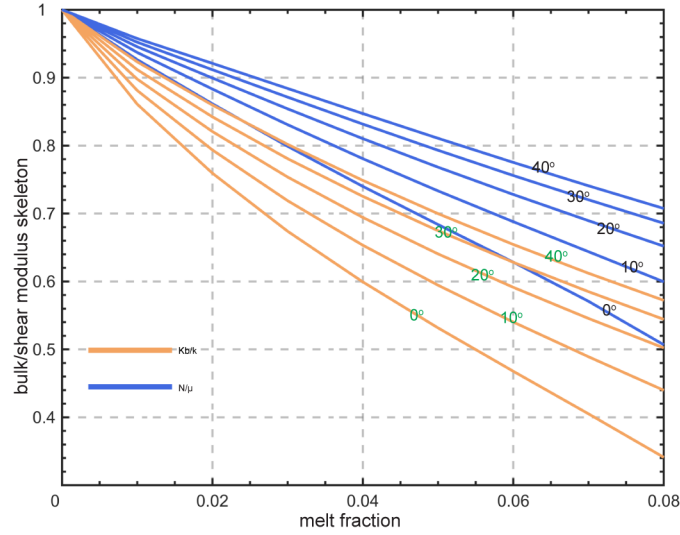
Extended Data Figure 7 | Normalized bulk modulus (K_b/k) and shear modulus (N/μ) of skeleton versus melt fraction. The ratios of wet and dry of bulk/shear modulus are decreasing with melt fraction. The numbers show on the lines are dihedral angles.

* manuele.faccenda@unipd.it